Article

Spatiotemporal Pattern of Invasive *Pedicularis* in the Bayinbuluke Land, China, during 2019–2021: An Analysis Based on PlanetScope and Sentinel-2 Data

Wuhua Wang [1], Jiakui Tang [1,2,*], Na Zhang [1,2], Yanjiao Wang [1], Xuefeng Xu [1,3] and Anan Zhang [1]

1 College of Resources and Environment, University of Chinese Academy of Sciences, Beijing 100049, China; wangwuhua20@mails.ucas.ac.cn (W.W.); zhangna@ucas.ac.cn (N.Z.); wangyanjiao21@mails.ucas.ac.cn (Y.W.); xuxuefeng18@mails.ucas.ac.cn (X.X.); zhanganan19@mails.ucas.ac.cn (A.Z.)
2 Yanshan Earth Key Zone and Surface Flux Observation and Research Station, University of Chinese Academy of Sciences, Beijing 101408, China
3 Precision Agriculture Lab, School of Life Sciences, Technical University of Munich, 85354 Freising, Germany
* Correspondence: jktang@ucas.ac.cn

Abstract: The accurate identification and monitoring of invasive plants are of great significance to sustainable ecological development. The invasive *Pedicularis* poses a severe threat to native biodiversity, ecological security, socioeconomic development, and human health in the Bayinbuluke Grassland, China. It is imperative and useful to obtain a precise distribution map of *Pedicularis* for controlling its spread. This study used the positive and unlabeled learning (PUL) method to extract *Pedicularis* from the Bayinbuluke Grassland based on multi-period Sentinel-2 and PlanetScope remote sensing images. A change rate model for a single land cover type and a dynamic transfer matrix were constructed under GIS to reflect the spatiotemporal distribution of *Pedicularis*. The results reveal that (1) the PUL method accurately identifies *Pedicularis* in satellite images, achieving F1-scores above 0.70 and up to 0.94 across all three datasets: PlanetScope data (seven features), Sentinel-2 data (seven features), and Sentinel-2 data (thirteen features). (2) When comparing the three datasets, the number of features is more important than the spatial resolution in terms of use in the PUL method of *Pedicularis* extraction. Nevertheless, when compared with PlanetScope data, Sentinel-2 data demonstrated a higher level of accuracy in predicting the distribution of *Pedicularis*. (3) During the 2019–2021 growing season, the distribution area of *Pedicularis* decreased, and the distribution was mainly concentrated in the northeast and southeast of Bayinbuluke Swan Lake. The acquired spatiotemporal pattern of invasive *Pedicularis* could potentially be used to aid in controlling *Pedicularis* spread or elimination, and the methods proposed in this study could be adopted by the government as a low-cost strategy to identify priority areas in which to concentrate efforts to control and continue monitoring *Pedicularis* invasion.

Keywords: *Pedicularis*; positive and unlabeled learning; dynamic variation; change detection; PlanetScope

1. Introduction

The Bayinbuluke Grassland, which is the second largest grassland in China, boasts a diverse array of grassland species and maintains a relatively intact ecosystem, providing a favorable habitat for various animals [1]. In recent years, the invasion of *Pedicularis* has significantly impacted animal husbandry and the ecological environment of the Bayinbuluke Grassland. *Pedicularis*, with its gorgeous appearance, is a poisonous grass and a semi-parasitic plant that has rapidly spread in alpine grasslands throughout western China [2]. The invasion of non-native grasses such as *Pedicularis* can cause a drastic alteration in ecosystems, leading to significant socioeconomic costs [3]. Therefore, local authorities must

urgently investigate the spatial and temporal patterns of *Pedicularis* invasion and develop effective management strategies to control this toxic plant species.

Previous studies have reported that *Pedicularis* had affected an area of 2.33×10^4 hm^2, which expanded to 3.30×10^3 hm^2, from 2000 to 2008 in the Bayinbuluke Grassland [4]. In 2018, Hejing County, Xinjiang Province, strived for CNY 7 million of funding for the *Pedicularis* control project to manually eradicate 2093.33 hm^2 of pastureland *Pedicularis*. The local government invested a significant amount of financial and labor resources into limiting the invasion of *Pedicularis* through physical, chemical, and biological means [5]. The traditional method of field surveying grassland species requires considerable human, material, and financial resources, and fieldwork makes ensuring quality and efficiency challenging [6,7]. Currently, remote sensing technology has significant advantages for dynamically monitoring and analyzing vast grassland resources and their ecological environments [8]. However, only one related study has been conducted on the identification of *Pedicularis* in the Bayinbuluke Grassland using satellite images, and the applied method did not perform well. Gao. S [9] studied the distribution of *Pedicularis* in 2016 using a maximum likelihood algorithm based on GaoFen-1 WFV with a spatial resolution of 16 m; they achieved a low precision of 80.91%, and a large number of samples were required for labeling. Therefore, here, we demonstrate an innovative application of high-resolution remote sensing imagery to discern the invasive species *Pedicularis* by employing the PUL method. Furthermore, we conduct a comprehensive assessment aimed at precisely outlining the advantages and limitations associated with the utilization of various remote sensing images for Pedicularis extraction.

Supervised classification algorithms, such as maximum likelihood, decision trees, support vector machine (SVM), random forest, and deep neural networks, have been widely used for land use and cover classification. Their performance has been validated in previous studies [10–12]. However, these algorithms require labeling all land cover types, which can be a tremendous drain on resources when only one specific land cover type is of interest [13]. Therefore, there is a growing need to develop one-class classifiers that can extract specific land cover types using only feature data of the target of interest. Several one-class classifiers have been proposed, including one-class SVM, isolation forest, and naive Bayes classifier [14–16]. In addition to labeled samples, unlabeled samples can provide useful information for constructing classifiers. Positive and unlabeled learning (PUL), a special one-class classification approach, has been increasingly improved upon and has demonstrated improved land cover classification accuracy in recent years [17]. Previous studies have mainly applied PUL and one-class classification to identify features such as urban buildings, large land targets, and rivers [18–20]. A UAV-based study found that the PUL approach was more appropriate for accurate *Pedicularis* extraction, suggesting its potential as a promising approach for single-species extraction [21]. Owing to the sporadic distribution pattern of *Pedicularis*, the reflectance characteristics of the pixel bands in remote sensing images with lower resolutions showed reduced spectral purity, thereby posing challenges to accurate identification endeavors. Compared with other measurements, both PlanetScope and Sentinel-2, as multi-spectral instruments, exhibit superior spatial resolution and better temporal revisit capabilities. This attribute renders them a judicious choice for Pedicularis identification.

Remote sensing image change monitoring is a technique that quantitatively analyzes and determines the process and characteristics of feature changes based on remote sensing images of the same area over different periods [22]. It is widely used in disaster assessment, urban development, and land use/cover [23]. Common methods for change monitoring include the image difference method, the image ratio method, the principal component transform method, the vegetation index method, and post-classification comparison [24]. To improve the temporal transfer of the algorithm, we selected unlabeled samples from multiple periods. The change-detection-based sample transfer approach is efficient, simple, and robust and has the potential to be used in large-scale ground cover classification [25–27]. This study takes advantage of PUL's ability to conserve negative sample information, reduc-

ing the statistical distribution differences between images of the target area by identifying areas of invariance between multiple temporal images [28], and combining the change-detection and post-classification approaches to solve the image classification problem of the target area [29]. A post-classification comparison is the most direct method of change monitoring. The advantage of this method is that it avoids the image sequence consistency conditions required for the direct comparison method, as well as avoids image radiation correction and matching problems. However, this method requires the development of uniform classification criteria enforced via image classification [30,31]. This method is extremely dependent on the accuracy of the classification algorithm, but this method performs well when analyzing the variation in a single species [32]. Therefore, this research uses a post-classification change detection approach for the analysis [33].

The aim of this study was to employ remote sensing techniques to obtain the temporal and spatial distribution of *Pedicularis* in Swan Lake and the buffer zone of the Bayinbuluke Grassland. Remote sensing data were collected in August for three consecutive years (2019–2021) to facilitate a comparison of the changes over time. Geospatial information holds valuable and significant data useful for the strategic planning of eradication efforts targeting *Pedicularis* infestations. Our objectives are as follows:

(1) Assessing the accuracy of PUL on predictions of the poisonous species *Pedicularis*;
(2) Comparing the efficacy of Sentinel-2 and PlanetScope satellite imagery in the identification of *Pedicularis*;
(3) Generating precise distribution maps of *Pedicularis* with time-series data for subsequent spatiotemporal analysis to support the conservation of the Bayinbuluke Grassland ecosystem through time-series remote sensing dynamic monitoring.

This paper is structured as follows. Section 2 describes the materials and methods, including the dataset used for the study, the principles of the PUL method, and the scheme for extending PUL for land cover classification and change detection. Section 3 presents the experimental results, including a comparison of the two types of data sources. Section 4 discusses the issue of change detection and the obtained results. Finally, Section 5 draws some conclusions.

2. Materials and Methods

All calculations and analyses of the research were performed in Python (v3.6.12) and the geographic information system ArcGIS (v10.6, ESRI). The experiment was run on Windows 10 on a machine with two 36-core Intel Xeon 3.10 GHz processors and 128 GB RAM. The technology workflow of the study has been organized in the following sections (Figure 1).

2.1. Study Area

The Bayinbuluke Grassland (42°18′~43°34′N, 82°27′~86°17′E), in the southern hinterland of the central part of Mountain Tianshan, is located in the northwest region of Hejing county in Xinjiang Province [34]. Furthermore, it is the second largest grassland in China and the most extensive subalpine, alpine meadow grassland in the desert region of China, with a total area of 3523.94 km^2 [35,36], and the main vegetation types are alpine grassland and swampy alpine meadows [37]. The Bayinbuluke Grassland is part of the Kaidu River basin, where water comes mainly from alpine snow melting and the recharge of natural precipitation. Its altitude is 2400~4400 m; the average annual temperature is −4.7 °C, with an extreme high of 28.3 °C and an extreme low of −48.1 °C; the annual precipitation is 216.8~361.8 mm; it experiences about 150~180 d of snow; and the annual dry grass period is seven months. Due to the cold weather, the soil in this area is frozen and there are almost no large trees. There are six main land use types in this grassland: high-cover pasture, low-cover pasture, marshland, timberland, water, and wild land. The water areas include rivers and lakes in the grassland and mountain snowfields [34]. The study area is shown in Figure 2.
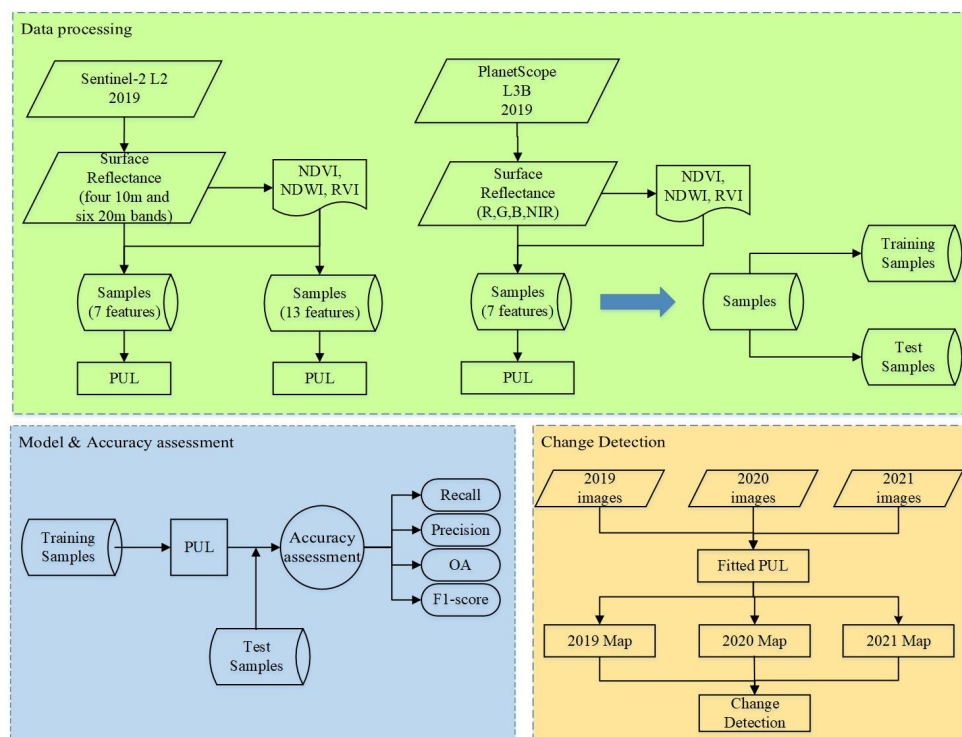
Figure 1. The technology workflow of the study (Blue arrows refer to the components of Samples).

2.2. Data Sources

2.2.1. UAV RGB Imagery

Selecting samples through a visual interpretation of remote sensing images with a low spatial resolution (relative to UAV images) presents a challenge due to the varying degrees of sparsity in the distribution of *Pedicularis* across different regions. Therefore, this study selected *Pedicularis* samples on satellite images via visual interpretation with the aid of UAV RGB (380~760 nm) imagery, which was obtained using a SONY RX1RII. The UAV data selected for the study area were taken on 7 August (f), 8 August (c), and 9 August (d, e), 2019 (Figure 2). The UAV was a DJI M600 (DJI, Shenzhen, China), and the flight information was planned in DJI GS Pro. The flight height of the UAV was 230 m, and the forward and side overlaps were 80% and 70%, respectively. The spatial resolution of all images acquired was 3 cm. The areas photographed by the UAV and where it was located are shown in Figure 2.

2.2.2. Sentinel-2 Imagery

The Sentinel-2 L2-level product used in the study was a Sentinel-2 Multispectral Instrument (MSI) from the European Space Agency (ESA). Sentinel-2 images cover 13 spectral bands in the visible, near-infrared (NIR), and short-wave infrared (SWIR) wavelengths, with four bands at 10 m, six bands at 20 m, and three bands at 60 m spatial resolution. The characteristics of the bands are listed in Table 1. For Sentinel-2 data, four 10 m and six 20 m bands can be used for land cover/land use (LCLU) mapping and change detection. The Sentinel-2 L2-level product provides the surface reflectance of images [38]. Regarding the matching of imaging data, imaging quality, and imaging time, through the Google Earth Engine platform, this study screened remote sensing images from 1 August to 31 August 2019. In order to obtain a better surface reflectance product, the Sentinel-2 L2-level product needs to be filtered and pre-processed. This experiment selected images with less than 10% cloudiness and filled the filtered images via temporal interpolation. Next, the filtered images were mosaicked and clipped through the region of interest (ROI) and all bands were resampled to 10 m. The sensor configuration of Sentinel-2 is as follows [39].
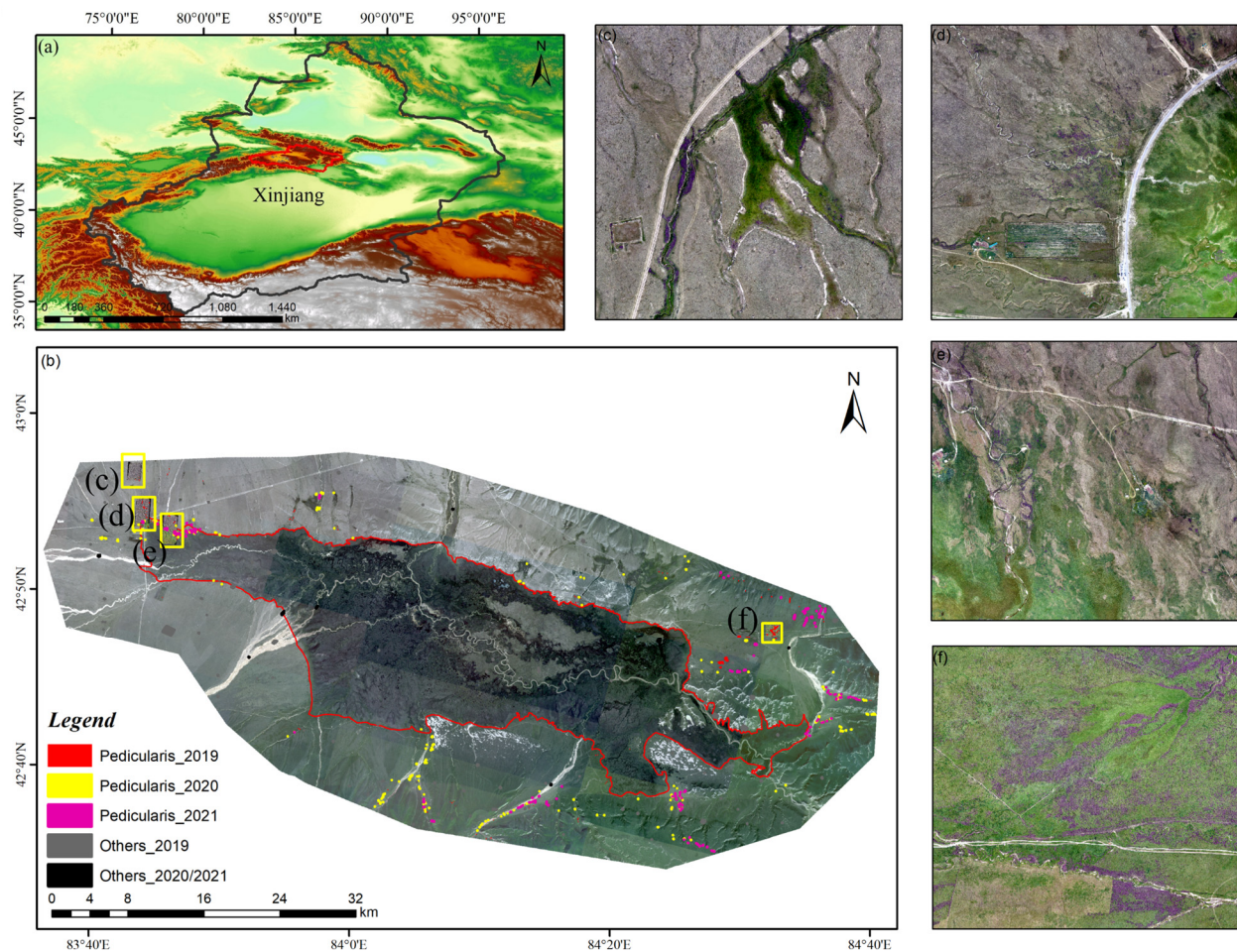
Figure 2. Location of the study area. (**a**) The study area is located in Hejing County, Xinjiang Province, China. (**b**) The Swan Lake (red boundary) and its buffer zone in the Bayinbuluke Grassland (background: an RGB remote sensing image acquired from PlanetScope in August 2019). (**c**–**f**) Orthomosaic image taken via an RGB UAV in August 2019 (the purple pixels are *Pedicularis*).

Table 1. Configuration information for the Sentinel-2 satellite.

Band Name	Sentinel-2A/Sentinel-2B Central Wavelength (nm)	Resolution (Meters)
Band 1—Coastal aerosol	443.9/442.2	60
Band 2—Blue	496.6/492.1	10
Band 3—Green	560.0/559.0	10
Band 4—Red	664.5/664.9	10
Band 5—Vegetation red edge	703.9/703.8	20
Band 6—Vegetation red edge	740.2/739.1	20
Band 7—Vegetation red edge	782.5/779.7	20
Band 8—NIR	835.1/832.9	10
Band 8A—Narrow NIR	864.8/864.0	20
Band 9—Water Vapor	945.0/943.2	60
Band 10—SWIR–Cirrus	1373.5/1376.9	60
Band 11—SWIR	1613.7/1610.4	20
Band 12—SWIR	2202.4/2185.7	20

The 60 m spatial resolution bands were not used in the experiment.

2.2.3. PlanetScope Imagery

The PlanetScope images with a 3 m spatial resolution were from the Planet Labs. It had four reflectance bands—blue, green, red, and near-infrared—with near-daily global

coverage. The PlanetScope images can be accessed for free by researchers through a research and education license (https://developers.planet.com/ (accessed on 1 May 2022)). This study used a Level-3B surface reflectance product, which was geometrically corrected, radiometrically corrected, and atmospherically corrected. We also processed it with ENVI (v5.3, ESRI) for mosaic, registration, and reflectance calculations (divided by 10,000). The daily acquisition of PlanetScope data allowed us to select images with optimal imaging quality for our analysis. For our experiment, we selected PlanetScope images from 7 August and 12 August 2019. Similarly, for the year 2020, we selected images acquired on 5 August, 24 August, and 30 August. For the year 2021, we selected images acquired on 11 August, 18 August, and 23 August. The configuration information for the PlanetScope satellite is as Table 2 [40].

Table 2. Configuration information for the PlanetScope satellite.

Band Name	Spatial Resolution (m)	Spectral Wavelength (nm)
Blue		464–517
Green		547–585
Red	3.0	650–682
NIR		846–888

2.3. Datasets and Data Analysis

2.3.1. Generation of Additional Features

Identifying *Pedicularis* on satellite images is a challenging operation. It is difficult to identify *Pedicularis* accurately through object-oriented methods. Therefore, it is necessary to use pixel-based classification to extract *Pedicularis*, and feature engineering is a particularly useful method. Some work in the literature has indicated that spectral features and combined vegetation indices are more essential than textural features and principal components in target identification and classification [41,42].

In order to better extract *Pedicularis* from the land cover, we compared the spectral characteristics of *Pedicularis* and familiar grasses. These spectral curves were obtained from the results in a previous study [43]. The normalized difference vegetation index (NDVI), the normalized ratio vegetation index (RVI), and the difference water index (NDWI) were obtained using Equations (1)–(3), respectively. The NDVI is one of the most influential parameters for characterizing changes in vegetation greenness, and it is often employed in studies of land cover [44]. RVI is widely used to estimate and monitor the biomass of green plants [45]. *Pedicularis* is a water-loving plant, often growing next to rivers [4,46]. Therefore, this experiment calculated the NDWI to extract *Pedicularis* [47]. Numerous studies have verified that the three indices are efficient for land use/land cover and target extraction [44,45,48–51].

$$NDVI = \frac{\rho_{nir} - \rho_{red}}{\rho_{nir} + \rho_{red}} , \tag{1}$$

$$RVI = \frac{\rho_{nir}}{\rho_{red}} , \tag{2}$$

$$NDWI = \frac{\rho_{green} - \rho_{nir}}{\rho_{green} + \rho_{nir}} . \tag{3}$$

2.3.2. Construction of the Datasets

This study was based on UAV RGB images from the PlanetScope and Sentinel-2 satellites, with visual interpretation using ROIs plotted on the UAV RGB images to select the *Pedicularis* samples. These data were obtained in August for each of the years 2019~2021, and the details are presented in Section 2.2. Subsequently, we selected a sample of non-*Pedicularis* species for 2019 to 2021, ensuring that the chosen locations exhibited a consistent distribution of non-*Pedicularis* species in 2020 and 2021. Finally, the samples used as input data for the construction of the model were of three types: PlanetScope data (7 features),

Sentinel-2 data (7 features), and Sentinel-2 data (13 features). The sample information is shown in Table 3. The location of the sample selection is shown in Figure 2b.

Table 3. Ground sample information for the study regions.

		Training Samples (Pixels)		Test Samples (Pixels)	
		Pedicularis	**Others**	*Pedicularis*	**Others**
2019	Sentinel-2 data (7/13 features)	7690	7690	1923	5598
	PlanetScope data (7 features)	62,063	62,063	15,515	455,615
2020	Sentinel-2 data (7/13 features)	1943	6477	486	1900
	PlanetScope data (7 features)	15,568	51,893	15,515	15,434
2021	Sentinel-2 data (7/13 features)	2395	7983	599	1900
	PlanetScope data (7 features)	19,520	65,066	4880	15,434

Others: unlabeled samples. Seven features: four 10 m bands and three vegetation indices. Thirteen features: four 10 m, six 20 m bands, and three vegetation indices.

The constructed models were applied to three different datasets for change detection in multi-period remotely sensed images. The classification results were evaluated and analyzed separately, and the samples were partitioned into training and test sets at an 8:2 ratio. To ensure balance within the training set, we performed downsampling such that the proportion of positive class samples to unlabeled samples was 3:7 in 2020/2021. Since the sample size in 2019 was sufficient, 1:1 was chosen for modelling to ensure the model's generalizability. The details of the selected samples are shown in Table 3.

2.4. Methodology

2.4.1. Classification Method

This study used the PUL method, which was demonstrated to be feasible for identifying *Pedicularis* in another study [21]. This method is based on the bootstrap aggregation (bagging) technique: the algorithm iteratively trains many binary classifiers to distinguish known positive (P) examples from random subsamples of the unlabeled (U) dataset and to average their predictions. PUL is a semi-supervised learning algorithm based on a positive and unlabeled sample [52]. This study chose decision trees as the base classifiers and described PUL's classification results in detail. Similar to all machine learning approaches, the PUL methodology encounters challenges in addressing the intricacies of spatiotemporal migration within the recognition process. However, this algorithm is a few-shot learning approach, which is well-suited for addressing the challenge of identifying *Pedicularis* in the presence of limited samples, particularly within a vast spatial extent.

The steps are as follows: (1) determine a set of reliable negation (RN) examples, which has a small number of positive samples, from U and transform the problem into a binary classification problem; (2) train binary classifiers based on P and RN by iteratively applying existing classification algorithms; and (3) iterate over the previous two steps, with the number of bootstrap samples T also being a user-defined parameter. Finally, the probability of each unlabeled sample being judged as a positive sample is calculated.

In the PUL classifier, positive and negative samples are selected from the training dataset to train the model. In an example conducted in 2019, Sentinel-2 had 7690 positive and 7690 negative samples. To improve the training efficiency of PUL, we trained 'n' decision trees to fit the training dataset. Firstly, we selected 10% of the positive class samples as positive samples (y = 1); secondly, the remaining 90% of positive class samples and all negative class samples were labeled as unlabeled samples (y = 0); then, the same proportion of unlabeled samples was randomly selected as negative samples (y = −1) for training; and, finally, 'k' iterations were performed in this manner. The probability of each sample being positive was calculated to obtain the classification result of this classifier. The parameter 'k' was adjusted from 100 to 2000 with a step size of 100. The 'n' ranged from 100 to 1000 with a step size of 100. PlanetScope datasets were modelled using the same methodology and range of parameters.

2.4.2. Accuracy Assessment

Using PUL, we obtained a confusion matrix and calculated the evaluation metrics on the test dataset, including recall, precision, overall accuracy (OA), F1-score, and AUC (area under the ROC curve), which can be calculated using the ROC curve (receiver operating characteristic curve). These metrics were utilized to assess the model's performance. Precision represents predictions for a positive class in the truly labeled dataset and can be obtained using Equation (4). Recall represents the evaluation of samples predicted to be in the positive class and can be obtained using Equation (5). Overall accuracy (OA) is the sum of the true positives plus true negatives divided by the total number of tested individuals, as shown in Equation (7). F1-score is a metric that combines the strengths of precision and recall, is well suited for evaluating models in situations where there is an imbalance between categories, and can be calculated using Equation (8). AUC can be viewed as the probability of randomly selecting a pair of positive and negative samples from a sample, which is the area under the ROC curve drawn using the FPR and TPR (Equations (5) and (6)). The AUC is less sensitive to class imbalance than OA and reflects the model's performance under sample imbalance more accurately [53].

$$precision = \frac{TP}{TP + FP} , \tag{4}$$

$$TPR = recall = \frac{TP}{TP + FN} , \tag{5}$$

$$FPR = \frac{FP}{TN + FP}. \tag{6}$$

$$OA = \frac{TP + TN}{TP + TN + FP + FN} , \tag{7}$$

$$F1 - score = \frac{2 \times precision \times recall}{precision + recall} \tag{8}$$

TP, *FP*, *FN*, and *TN* are the classifications true positive, false positive, false negative, and true negative, respectively.

2.4.3. Change Detection

This study took the distribution area and proportion, and the change rate of *Pedicularis* from the classification results for 2019–2021 [54]. To further reflect the direction, amount, and rate of *Pedicularis* change, this study generated a dynamic transfer matrix from the change detection results in 2019–2021, which can reflect the flow of species change [55]. Based on these results, we analyzed the change in the dynamics of *Pedicularis*. The change rate of the area of *Pedicularis* was calculated using Equation (8).

$$C_i = \frac{W_{bi} - W_{ai}}{W_{ai}} \times \frac{1}{t} \times 100\% . \tag{9}$$

where C_i is the change rate of *Pedicularis* during the study period; W_{ai} and W_{bi} are the distribution areas of *Pedicularis* at the beginning and end of the study period, respectively; t is the study period, measured by year; and the calculation results indicate the annual change rate of *Pedicularis* [56].

A transfer matrix model can depict a species' evolutionary patterns, capturing both species distribution changes and their migration directions. Using the classification outcomes of the study area in 2019, 2020, and 2021, we derived the transfer areas for each stage and constructed a transfer matrix.

$$S_{ij} = \begin{bmatrix} S_{11} & \cdots & S_{1n} \\ \vdots & \ddots & \vdots \\ S_{n1} & \cdots & S_{nn} \end{bmatrix}. \tag{10}$$

where S is the species area; i and j are the species types at the beginning and end of the study, respectively; and n is the number of species types.

3. Results

3.1. Comparison of Classification Accuracy on Sentinel-2 and PlanetScope

Three classifiers were developed for the positive and unlabeled learning (PUL) method using three different types of datasets. Based on the results presented in Table 4, the highest extraction accuracy for *Pedicularis* was observed when using Sentinel-2 data (13 features), yielding an F1-score of 0.9405. On the other hand, the lowest classification accuracy was obtained using PlanetScope data, resulting in an F1-score of 0.7049. Notably, the classification accuracy for *Pedicularis* using Sentinel-2 data (7 features) was significantly higher compared with that obtained using PlanetScope data and slightly lower than the accuracy observed for Sentinel-2 data (13 features).

Table 4. Assessment metrics of models during the 2019–2021 period.

Year	Datasets	Types	Metrics			
			Recall	Precision	Accuracy	F1-Score
2019	Sentinel-2 data (7 features)	*Pedicularis*	0.9212	0.9286	0.9617	0.9248
		Others	0.9757	0.9730		
	Sentinel-2 data (13 features)	*Pedicularis*	0.9278	0.9536	0.9700	0.9405
		Others	0.9845	0.9754		
	PlanetScope data (7 features)	*Pedicularis*	0.8458	0.6042	0.8678	0.7049
		Others	0.8728	0.9610		
2020	Sentinel-2 data (7 features)	*Pedicularis*	0.8861	0.7307	0.9169	0.8009
		Others	0.9241	0.9721		
	Sentinel-2 data (13 features)	*Pedicularis*	0.8710	0.9045	0.9583	0.8874
		Others	0.9786	0.9702		
	PlanetScope data (7 features)	*Pedicularis*	0.8340	0.6132	0.8708	0.7067
		Others	0.8793	0.9584		
2021	Sentinel-2 data (7 features)	*Pedicularis*	0.8971	0.8629	0.9454	0.8796
		Others	0.9591	0.9703		
	Sentinel-2 data (13 features)	*Pedicularis*	0.8864	0.9277	0.9593	0.9065
		Others	0.9802	0.9678		
	PlanetScope data (7 features)	*Pedicularis*	0.8985	0.7399	0.9313	0.8115
		Others	0.9377	0.9791		

Our findings indicate that the highest classification accuracy for *Pedicularis* was observed in 2019. While recall and precision were generally comparable across most models, recall was found to be higher than precision for the models built using PlanetScope data. Moreover, our results demonstrate that the difference between accuracy and F1-score is minimal when the model's accuracy is high but becomes more pronounced when the accuracy is low.

To evaluate the temporal transferability of the model, we tested the model developed in 2019 on data from 2020 and 2021. As illustrated in Figure 3, the model's performance on this test was unsatisfactory, with the F1-scores for both years being less than 0.62. Specifically, the F1-score for the PlanetScope dataset in 2020 was insufficient, with a value of only 0.3300. Subsequently, upon training the model with the corresponding year's training set, a notable improvement in accuracy was observed. These results demonstrate the potential of positive and unlabeled learning (PUL) for small-sample learning.
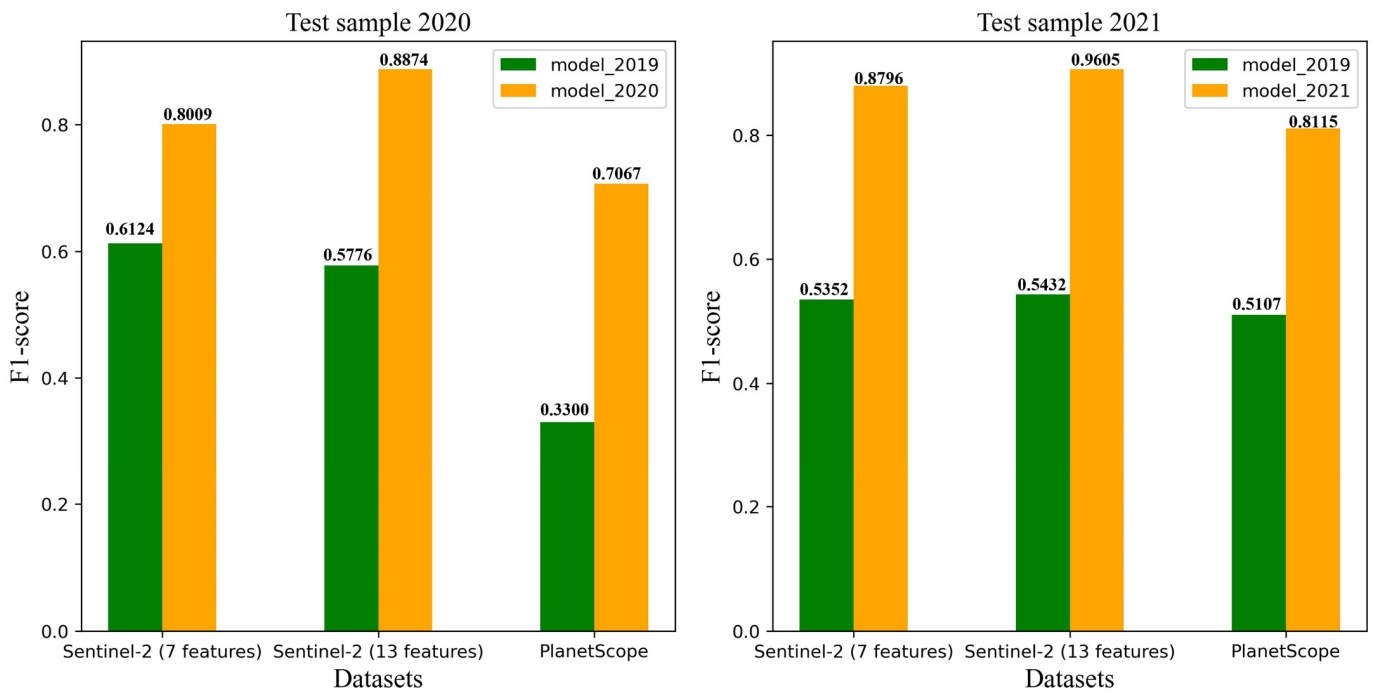
Figure 3. Comparison of accuracy between the 2019 model and model built in the same year as the test set.

As evidenced by the ROC and AUC curves depicted in Figure 4, changes in precision and recall exhibit an inverse relationship while the AUC values remain stable. In order to maximize the AUC, we could appropriately adjust the threshold to manipulate the precision and recall, ultimately achieving a balance between the two for accurate classification of *Pedicularis*. However, in scenarios with a large F1-score and accuracy gap, the AUC of the model remains low compared with that of other models.
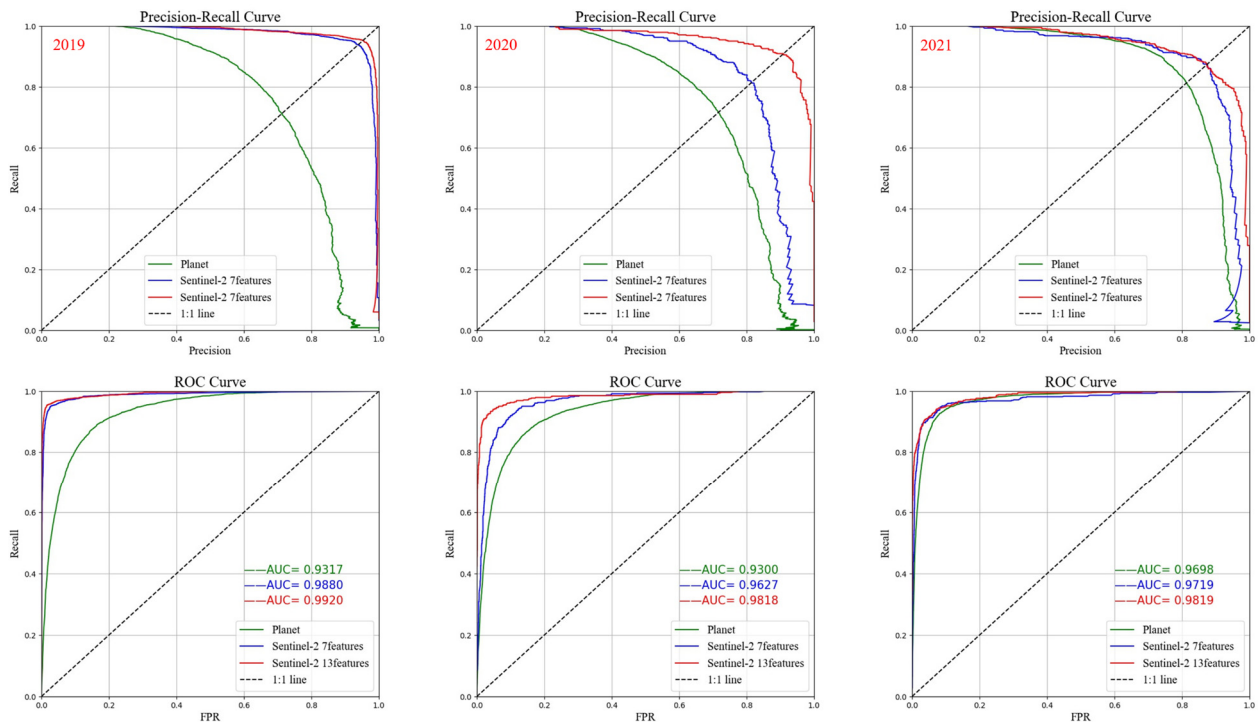

Figure 4. ROC and AUC curves for the models developed from 2019 to 2021.

3.2. Changes in Dynamics of Pedicularis

The classification results obtained using Sentinel-2 data (13 features) were the most accurate among all models. Accordingly, changes in the distribution area of *Pedicularis* from 2019 to 2021 were monitored based on this classification result. The analysis revealed that *Pedicularis* had the largest area, 195.7803 km^2, in 2019, accounting for 5.55% of the total region, while its size decreased to 3.54% in 2020.

Figure 5 illustrates the spatiotemporal distribution of *Pedicularis* from 2019 to 2021 using Sentinel-2 data (13 features). The results showed a gradual decrease in its distribution in the northwest and an increase in the south over the past three years. Additionally, the total distribution area of *Pedicularis* showed a decreasing and then increasing trend over this period.
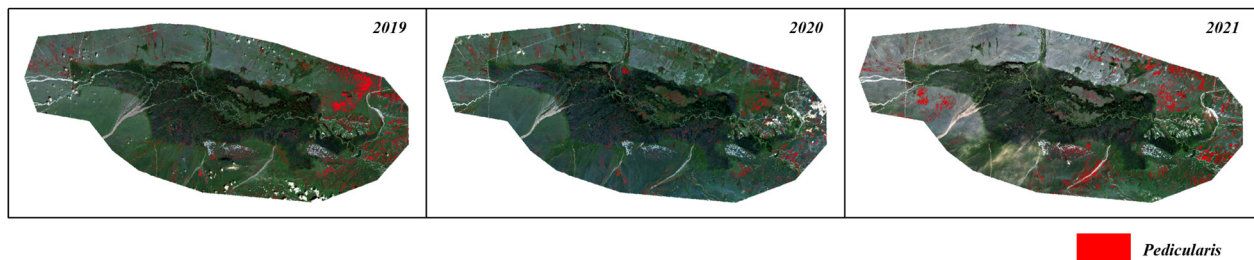

Figure 5. Spatiotemporal pattern of *Pedicularis* in 2019–2021 using Sentinel-2 data (13 feature).

The change in the distribution area of *Pedicularis i*n the Bayinbuluke Grassland was analyzed from 2019 to 2021. Comparing the changes in *Pedicularis* in 2019 and 2020, it was observed that 173.89 km^2 of the *Pedicularis* distribution area disappeared, while 103.0704 km^2 was converted from distribution areas of other species to that of *Pedicularis*, indicating an overall improvement. From 2020 to 2021, there was a decrease of 106.0108 km^2 in *Pedicularis*, followed by an increase of 138.2587 km^2. However, the total amount of *Pedicularis* from 2019 to 2021 still decreased, with a decrease in distribution area of 38.5740 km^2.

4. Discussion

4.1. Influencing Factors of Classification Accuracy

We can identify *Pedicularis* clearly from the high-resolution drone images. However, the low spatial resolution of the images and the interplay of spectral information from different land covers produce mixed pixels. These phenomena result in the color and geometric textural information of *Pedicularis* not being easily acquired on satellite images. The PUL method used in this study can effectively improve the classification accuracy of *Pedicularis* based on satellite imagery; relevant studies on UAV imagery can support this method [21].

During the mosaicking of data, an uneven color balance across multiple images can have an impact on the outcome of image classification [57]. Sentinel-2 only requires two images to be sufficient to cover the study area; PlanetScope has a higher temporal resolution and a smaller coverage area per image. It requires 41 images to cover the study area, making the classifier more likely to learn some noise.

The accuracy of *Pedicularis* extraction was significantly enhanced by increasing the number of features from 7 to 13 in the Sentinel-2 classification results. This finding aligns with other pixel-based classification methods [58]. Moreover, the classification results of the model constructed using Sentinel-2 data (13 features) provide a more realistic distribution of *Pedicularis*.

Comparing the identification results of PlanetScope data (seven features) and Sentinel-2 data (seven features), the identification result for the 10 m resolution is higher than that for the 3 m resolution, which is unexpected. Our analysis shows that this is mainly caused by the significant difference in spectral reflectance between the images due to PlanetScope

requiring more images [59,60]. Additionally, the band characteristics of the pixels are contingent on the complexity of the species within each pixel: the more intricate the object within the pixel, the greater the divergence between its spectral features and the pure pixel features, resulting in the reduced recognition accuracy of scattered patterns. Conversely, during sample selection, we noticed that Pedicularis was easier to identify in Sentinel-2 images compared to PlanetScope images, based solely on color considerations.

It has been found that the spectral signature of the same object using the same sensor may vary at different times, and this phenomenon also affects the classification results. Consequently, identifying features resistant to temporal and spectral variations is crucial for pixel-based classification methods, and can also help to improve the reliability of monitoring changes after classification.

4.2. Spatiotemporal Pattern of Pedicularis

Figure 5, Tables 5 and 6 collectively elucidate the dynamic trajectory of the spatial distribution of *Pedicularis* and characterize its temporal pattern, marked by an initial decrease, followed by a subsequent increase from 2019 to 2021. While the distribution of *Pedicularis* sharply decreased in the northwestern region between 2019 and 2020, other regions showed no significant migration trend. Furthermore, in 2021, the distribution area of *Pedicularis* in the southern region showed an increasing trend. As depicted in Figure 5, the distribution of *Pedicularis* was predominantly along rivers, suggesting that *Pedicularis* is a water-loving plant, which is consistent with local investigation findings [43]. Following a comprehensive survey, it has been observed that the precipitation levels in the region have exhibited a decline from 2019 to 2020. This observation explains the decrease also seen in the distribution of Artemisia marcescens [61]. This case also contributes to the investigation into the driving mechanisms underlying *Pedicularis* distribution. By utilizing GIS methods to analyze the spatial distribution of *Pedicularis*, a further understanding of its invasion routes and drivers can be attained.

Table 5. Statistics of distribution area of *Pedicularis* in different periods using Sentinel-2 data (13 features).

Year	Area (km^2)	Area Ratio (%)
2019	195.7803	5.55%
2020	124.9584	3.54%
2021	157.2063	4.46%

Table 6. Transition matrix of land cover change for 2019~2021.

	2019–2020		2020–2021		2019–2021	
	Pedicularis	Others	*Pedicularis*	Others	*Pedicularis*	Others
Pedicularis	21.8880	173.8923	18.9476	106.0108	33.6437	162.1330
Others	103.0704	3225.0944	138.2587	3260.7280	123.5590	3204.6058

This article discusses the feasibility of a spatiotemporal analysis based on PlanetScope and Sentinel-2 imagery. Both satellites have a high temporal resolution and meet the needs of long-time-series monitoring. However, post-classification change monitoring can avoid influencing the classification results due to different spatiotemporal and data sources. The accuracy of the classification results dramatically affects the detection of changes in the distribution of *Pedicularis*. It further shows that investigating a classifier or feature factor that can resist spatial and temporal variation and developing a better transfer learning method are essential.

4.3. A Case of Pedicularis Eradication

We learned that the government conducted a local campaign for the removal of *Pedicularis* in July 2019. To verify the process of eliminating *Pedicularis*, we looked up remote sensing images from PlanetScope, which has a high spatial resolution, for July 2019.

These images correspond to the position in Figure 2f. As seen from Figure 6, *Pedicularis* was physically removed by local people on 17 July, 23 July, and 29 July 2019. It is, therefore, essential to identify the location of *Pedicularis* and its dynamics. This contributes to the local government's efforts to control the invasion of *Pedicularis* and to protect the ecological environment [1,7].

Figure 6. Local variations in *Pedicularis* in PlanetScope images from July 2019 within the red box. (**a**–**c**) refer to PlanetScope images taken on 17 July, 23 July, and 29 July 2019. (the purple pixels are *Pedicularis*).

5. Conclusions

The main contribution of this work is the use of a new PUL method to extract *Pedicularis*. This extracted *Pedicularis* distribution is subsequently employed for the dynamic detection of Pedicularis and for conducting a spatiotemporal analysis of the prediction results. With the use of the spatial distribution of *Pedicularis* from 2019 to 2021, we can achieve real-time monitoring and the effective eradication of *Pedicularis*. In contrast to the one-class classifier, which only uses positive-class samples, PUL makes full use of numerous unlabeled samples to improve the accuracy of the classification results, contributing to curbing the expansion of the distribution area of poisonous *Pedicularis*. The conclusions are as follows:

(1) The proliferation of *Pedicularis* in the Bayinbuluke Grassland has resulted in significant ecological damage, necessitating the substantial expenditure of resources and efforts by the provincial government for rehabilitation efforts. In addressing this issue, change-detection methods utilizing remote sensing technology offer a practical approach for informed management and mitigation. Sentinel-2 images have the advantages of a large width, easily acquirable data, and high accuracy in extracting *Pedicularis*. The resolution of PlanetScope is higher than that of Sentinel-2, which is more advantageous when removing *Pedicularis* from small areas. The results of the study show that the PUL method is able to achieve a high recognition accuracy across different images.

(2) Within the confines of the same sensor platform, the influence of feature count on improvements to the identification accuracy becomes obvious with an ample sample size, as evidenced by an increasing feature count coinciding with increased recognition accuracy. However, within an equivalent feature framework, the correlation between resolution elevation and accuracy enhancement does not invariably hold, implying that the resultant classification outcome is dependent on the inherent data quality obtained using the sensor apparatus.

(3) The post-classification comparison algorithm avoids spectral differences in remote sensing images, especially long-time-series images from different sensors. It enables the rapid monitoring of regional variations in the distribution of different land types. However, it is highly dependent on the stability of the model, and a transferred, high-accuracy classification model needs to be further developed. The distribution of *Pedicularis* is concentrated in the northwestern and southwestern parts of Bayinbuluke

Swan Lake. From 2019 to 2021, the distribution area of *Pedicularis* exhibited a fluctuating trend, initially increasing and then subsequently decreasing, with the 2021 area measuring 157.2063 km^2. Despite better eradication efforts in the northeast region, the distribution area of *Pedicularis* did not exhibit significant changes, indicating that grassland managers may not have done enough to control the growth of *Pedicularis*.

Author Contributions: Methodology: W.W. and J.T.; validation: W.W., J.T. and N.Z.; formal analysis: W.W.; investigation: N.Z., Y.W. and J.T.; writing—original draft preparation: W.W.; writing—review and editing: W.W., J.T., X.X. and A.Z.; N.Z. contributed the same as the corresponding authors. All authors have read and agreed to the published version of the manuscript.

Data Availability Statement: Not applicable.

Conflicts of Interest: The authors declare no conflict of interest.

References

1. Fu, P.; Yao, J.; Hu, J.; Guo, X. Capital Endowments, Policy Perceptions and Herdsmen's Willingness to Reduce Livestock:A Case Study from the World Natural Heritage Site of Bayinbuluke. *Acta Agrestia Sin.* **2021**, *29*, 780–787.
2. Hameed, A.; Zafar, M.; Ahmad, M.; Sultana, S.; Bahadur, S.; Anjum, F.; Shuaib, M.; Taj, S.; Irm, M.; Altaf, M.A. Chemo-taxonomic and biological potential of highly therapeutic plant Pedicularis groenlandica Retz. using multiple microscopic techniques. *Microsc. Res. Tech.* **2021**, *84*, 2890–2905. [CrossRef] [PubMed]
3. Elkind, K.; Sankey, T.T.; Munson, S.M.; Aslan, C.E. Invasive buffelgrass detection using high-resolution satellite and UAV imagery on Google Earth Engine. *Remote Sens. Ecol. Conserv.* **2019**, *5*, 318–331. [CrossRef]
4. Sui, X.; Li, A.; Guan, K. Impacts of climatic changes as well as seed germination characteristics on the population expansion of Pedicularis verticillata. *Ecol. Environ. Sci.* **2013**, *22*, 1099–1104.
5. Yanyan, L.I.U.; Yukun, H.U.; Jianmei, Y.U.; Kaihui, L.I.; Guogang, G.A.O.; Xin, W. Study on Harmfulness of Pedicularis myriophylla and Its Control Measures. *Arid Zone Res.* **2008**, *25*, 778–782.
6. Hongtao, J.I.A.; Pingan, J.; Luming, C.; Chengyi, Z.; Yukun, H.U. Estimation of Organic Carbon Storage of Bayinbuluke Alpine Grassland Ecosystem. *Xinjiang Agric. Sci.* **2006**, *43*, 480–483.
7. Pingan, J.; Hui, L.I.; Hongtao, J.I.A.; Zihong, D. Impacts of fencing on soil animals diversity beneath mountainous lawn vegetation in Bayinbuluke. *J. Northwest Sci-Tech Univ. Agric. For.* **2007**, *35*, 69–74.
8. Choudhary, K.; Boori, M.S.; Kupriyanov, A. Landscape Analysis through Remote Sensing and GIS Techniques: A Case Study of Astrakhan, Russia. In Proceedings of the 8th International Conference on Graphic and Image Processing (ICGIP), Tokyo, Japan, 29–31 October 2016.
9. Gao, S.; Zheng, J.; Ma, T.; Wu, J.; Nasongcaoketu; Maidi, K. Research on the Applicability of Remote Sensing Monitoring of Inedible Grass Pedicularis sp. by GF-1 WFV Satellite in Bayanbulak Grassland. *Xinjiang Agric. Sci.* **2017**, *54*, 1949–1956.
10. Huber, N.; Ginzler, C.; Pazur, R.; Descombes, P.; Baltensweiler, A.; Ecker, K.; Meier, E.; Price, B. Countrywide classification of permanent grassland habitats at high spatial resolution. *Remote Sens. Ecol. Conserv.* **2023**, *9*, 133–151. [CrossRef]
11. Lopatin, J.; Dolos, K.; Kattenborn, T.; Fassnacht, F.E. How canopy shadow affects invasive plant species classification in high spatial resolution remote sensing. *Remote Sens. Ecol. Conserv.* **2019**, *5*, 302–317. [CrossRef]
12. Kakembo, V.; Smith, J.; Kerley, G. A Temporal Analysis of Elephant-Induced Thicket Degradation in Addo Elephant National Park, Eastern Cape, South Africa. *Rangel. Ecol. Manag.* **2015**, *68*, 461–469. [CrossRef]
13. Singh, P.S.; Singh, V.P.; Pandey, M.K.; Karthikeyan, S.; IEEE. One-class Classifier Ensemble based Enhanced Semisupervised Classification of Hyperspectral Remote Sensing Images. In Proceedings of the 2nd IEEE International Conference on Emerging Smart Computing and Informatics (ESCI), All India Shri Shivaji Memorial Soc, Inst Informat Technol, Pune, India, 12–14 March 2020; pp. 22–27.
14. Hossain, M.A.; Jia, X.; Benediktsson, J.A. One-Class Oriented Feature Selection and Classification of Heterogeneous Remote Sensing Images. *IEEE J. Sel. Top. Appl. Earth Obs. Remote Sens.* **2016**, *9*, 1606–1612. [CrossRef]
15. Li, W.; Guo, Q.; Elkan, C. A Positive and Unlabeled Learning Algorithm for One-Class Classification of Remote-Sensing Data. *IEEE Trans. Geosci. Remote Sens.* **2011**, *49*, 717–725. [CrossRef]
16. Mack, B.; Roscher, R.; Waske, B. Can I Trust My One-Class Classification? *Remote Sens.* **2014**, *6*, 8779–8802. [CrossRef]
17. Li, W.K.; Guo, Q.H. A maximum entropy approach to one-class classification of remote sensing imagery. *Int. J. Remote Sens.* **2010**, *31*, 2227–2235. [CrossRef]
18. Braun, A.C. Evaluation of One-Class Svm for Pixel-Based and Segment-Based Classification in Remote Sensing. In Proceedings of the ISPRS-Technical-Commission III Symposium on Photogrammetric Computer Vision and Image Analysis (PCV), Saint Mande, France, 1–3 September 2010; pp. 160–165.

19. Chang, S.; Du, B.; Zhang, L. A Subspace Selection-Based Discriminative Forest Method for Hyperspectral Anomaly Detection. *IEEE Trans. Geosci. Remote Sens.* **2020**, *58*, 4033–4046. [CrossRef]

20. Dambros, C.S.; Morais, J.W.; Azevedo, R.A.; Gotelli, N.J. Isolation by distance, not rivers, control the distribution of termite species in the Amazonian rain forest. *Ecography* **2017**, *40*, 1242–1250. [CrossRef]

21. Wang, W.; Tang, J.; Zhang, N.; Xu, X.; Zhang, A.; Wang, Y. Automated Detection Method to Extract Pedicularis Based on UAV Images. *Drones* **2022**, *6*, 399. [CrossRef]

22. Morshed, N.; Yorke, C.; Zhang, Q. Urban Expansion Pattern and Land Use Dynamics in Dhaka, 1989–2014. *Prof. Geogr.* **2017**, *69*, 396–411. [CrossRef]

23. Franklin, S.E.; Ahmed, O.S.; Wulder, M.A.; White, J.C.; Hermosilla, T.; Coops, N.C. Large Area Mapping of Annual Land Cover Dynamics Using Multitemporal Change Detection and Classification of Landsat Time Series Data. *Can. J. Remote Sens.* **2015**, *41*, 293–314. [CrossRef]

24. Angulo, D.; Angulo, F.; Olivar, G. Dynamics and Forecast in a Simple Model of Sustainable Development for Rural Populations. *Bull. Math. Biol.* **2015**, *77*, 368–389. [CrossRef] [PubMed]

25. Wu, T.J.; Luo, J.C.; Zhou, Y.N.; Wang, C.P.; Xi, J.B.; Fang, J.W. Geo-Object-Based Land Cover Map Update for High-Spatial-Resolution Remote Sensing Images via Change Detection and Label Transfer. *Remote Sens.* **2020**, *12*, 174. [CrossRef]

26. Yu, W.J.; Zhou, W.Q.; Qian, Y.G.; Yan, J.L. A new approach for land cover classification and change analysis: Integrating backdating and an object-based method. *Remote Sens. Environ.* **2016**, *177*, 37–47. [CrossRef]

27. Chen, X.H.; Chen, J.; Shi, Y.S.; Yamaguchi, Y. An automated approach for updating land cover maps based on integrated change detection and classification methods. *ISPRS-J. Photogramm. Remote Sens.* **2012**, *71*, 86–95. [CrossRef]

28. Qian, Y.G.; Zhou, W.Q.; Yu, W.J.; Han, L.J.; Li, W.F.; Zhao, W.H. Integrating Backdating and Transfer Learning in an Object-Based Framework for High Resolution Image Classification and Change Analysis. *Remote Sens.* **2020**, *12*, 4094. [CrossRef]

29. Xu, Y.D.; Yu, L.; Zhao, F.R.; Cai, X.L.; Zhao, J.Y.; Lu, H.; Gong, P. Tracking annual cropland changes from 1984 to 2016 using time-series Landsat images with a change-detection and post-classification approach: Experiments from three sites in Africa. *Remote Sens. Environ.* **2018**, *218*, 13–31. [CrossRef]

30. Feng, X.; Li, P.; Cheng, T. Detection of Urban Built-Up Area Change From Sentinel-2 Images Using Multiband Temporal Texture and One-Class Random Forest. *IEEE J. Sel. Top. Appl. Earth Obs. Remote Sens.* **2021**, *14*, 6974–6986. [CrossRef]

31. Kempeneers, P.; Sedano, F.; Strobl, P.; McInerney, D.O.; San-Miguel-Ayanz, J. Increasing Robustness of Postclassification Change Detection Using Time Series of Land Cover Maps. *IEEE Trans. Geosci. Remote Sens.* **2012**, *50*, 3327–3339. [CrossRef]

32. Crowson, M.; Hagensieker, R.; Waske, B. Mapping land cover change in northern Brazil with limited training data. *Int. J. Appl. Earth Obs. Geoinf.* **2019**, *78*, 202–214. [CrossRef]

33. Colditz, R.R.; Acosta-Velazquez, J.; Diaz Gallegos, J.R.; Vazquez Lule, A.D.; Teresa Rodriguez-Zuniga, M.; Maeda, P.; Cruz Lopez, M.I.; Ressl, R. Potential effects in multi-resolution post-classification change detection. *Int. J. Remote Sens.* **2012**, *33*, 6426–6445. [CrossRef]

34. Bao, A.; Cao, X.; Chen, X.; Xia, Y. Study on Models for Monitoring of Aboveground Biomass about Bayinbuluke grassland Assisted by Remote Sensing. In Proceedings of the Conference on Remote Sensing and Modeling of Ecosystems for Sustainability, San Diego, CA, USA, 13 August 2008.

35. Chen, X.; Yang, Z.; Wang, T.; Han, F. Landscape Ecological Risk and Ecological Security Pattern Construction in World Natural Heritage Sites: A Case Study of Bayinbuluke, Xinjiang, China. *ISPRS Int. J. Geo-Inf.* **2022**, *11*, 328. [CrossRef]

36. Xu, X.; Wang, X.; Zhu, X.; Jia, H.; Han, D. Landscape Pattern Changes in AlpineWetland of Bayanbulak Swan Lake during 1996–2015. *J. Nat. Resour.* **2018**, *33*, 1897–1911.

37. Liu, Q.; Yang, Z.P.; Han, F.; Shi, H.; Wang, Z.; Chen, X.D. Ecological Environment Assessment in World Natural Heritage Site Based on Remote-Sensing Data. A Case Study from the Bayinbuluke. *Sustainability* **2019**, *11*, 6385. [CrossRef]

38. Grabska, E.; Frantz, D.; Ostapowicz, K. Evaluation of machine learning algorithms for forest stand species mapping using Sentinel-2 imagery and environmental data in the Polish Carpathians. *Remote Sens. Environ.* **2020**, *251*, 112103. [CrossRef]

39. De Vroey, M.; de Vendictis, L.; Zavagli, M.; Bontemps, S.; Heymans, D.; Radoux, J.; Koetz, B.; Defourny, P. Mowing detection using Sentinel-1 and Sentinel-2 time series for large scale grassland monitoring. *Remote Sens. Environ.* **2022**, *280*, 113145. [CrossRef]

40. Kimm, H.; Guan, K.Y.; Jiang, C.Y.; Peng, B.; Gentry, L.F.; Wilkin, S.C.; Wang, S.B.; Cai, Y.P.; Bernacchi, C.J.; Peng, J.; et al. Deriving high-spatiotemporal-resolution leaf area index for agroecosystems in the US Corn Belt using Planet Labs CubeSat and STAIR fusion data. *Remote Sens. Environ.* **2020**, *239*, 111615. [CrossRef]

41. Holloway-Brown, J.; Helmstedt, K.J.; Mengersen, K.L. Interpolating missing land cover data using stochastic spatial random forests for improved change detection. *Remote Sens. Ecol. Conserv.* **2021**, *7*, 649–665. [CrossRef]

42. Saber, A.; El-Sayed, I.; Rabah, M.; Selim, M. Evaluating change detection techniques using remote sensing data: Case study New Administrative Capital Egypt. *Egypt. J. Remote Sens. Space Sci.* **2021**, *24*, 635–648. [CrossRef]

43. Gao, S.; Lin, J.; Ma, T.; Wu, J.; Zheng, J. Extraction and Analysis of Hyperspectral Data and Characteristics fromPedicularis on Bayanbulak Grassland in Xinjiang. *Remote Sens. Technol. Appl.* **2018**, *33*, 908–914.

44. Carlson, T.N.; Ripley, D.A. On the relation between NDVI, fractional vegetation cover, and leaf area index. *Remote Sens. Environ.* **1997**, *62*, 241–252. [CrossRef]

45. Gnyp, M.L.; Miao, Y.X.; Yuan, F.; Ustin, S.L.; Yu, K.; Yao, Y.K.; Huang, S.Y.; Bareth, G. Hyperspectral canopy sensing of paddy rice aboveground biomass at different growth stages. *Field Crops Res.* **2014**, *155*, 42–55. [CrossRef]

46. Wang, D.; Cui, B.C.; Duan, S.S.; Chen, J.J.; Fan, H.; Lu, B.B.; Zheng, J.H. Moving north in China: The habitat of Pedicularis kansuensis in the context of climate change. *Sci. Total Environ.* **2019**, *697*, 133979. [CrossRef] [PubMed]

47. Chai, L.; Jiang, H.; Crow, W.T.; Liu, S.; Zhao, S.; Liu, J.; Yang, S. Estimating Corn Canopy Water Content From Normalized Difference Water Index (NDWI): An Optimized NDWI-Based Scheme and Its Feasibility for Retrieving Corn VWC. *IEEE Trans. Geosci. Remote Sens.* **2021**, *59*, 8168–8181. [CrossRef]

48. Francini, S.; McRoberts, R.E.; Giannetti, F.; Mencucci, M.; Marchetti, M.; Mugnozza, G.S.; Chirici, G. Near-real time forest change detection using PlanetScope imagery. *Eur. J. Remote Sens.* **2020**, *53*, 233–244. [CrossRef]

49. Sui, Y.; Shao, F.; Wang, C.; Sun, R.; Ji, J. Complex network modeling of spectral remotely sensed imagery: A case study of massive green algae blooms detection based on MODIS data. *Phys. A-Stat. Mech. Its Appl.* **2016**, *464*, 138–148. [CrossRef]

50. Zhao, B.; Yang, F.; Zhang, R.; Shen, J.; Pilz, J.; Zhang, D. Application of unsupervised learning of finite mixture models in ASTER VNIR data-driven land use classification. *J. Spat. Sci.* **2021**, *66*, 89–112. [CrossRef]

51. Zhou, X.-X.; Li, Y.-Y.; Luo, Y.-K.; Sun, Y.-W.; Su, Y.-J.; Tan, C.-W.; Liu, Y.-J. Research on remote sensing classification of fruit trees based on Sentinel-2 multi-temporal imageries. *Sci. Rep.* **2022**, *12*, 11549. [CrossRef]

52. Mordelet, F.; Vert, J.P. A bagging SVM to learn from positive and unlabeled examples. *Pattern Recognit. Lett.* **2014**, *37*, 201–209. [CrossRef]

53. Halligan, S.; Altman, D.G.; Mallett, S. Disadvantages of using the area under the receiver operating characteristic curve to assess imaging tests: A discussion and proposal for an alternative approach. *Eur. Radiol.* **2015**, *25*, 932–939. [CrossRef] [PubMed]

54. Wang, L.; Zheng, S.; Wang, X. The Spatiotemporal Changes and the Impacts of Climate Factors on Grassland in the Northern Songnen Plain (China). *Sustainability* **2021**, *13*, 6568. [CrossRef]

55. Zhang, Z.; Yang, X.; Xie, F. Macro analysis of spatiotemporal variations in ecosystems from 1996 to 2016 in Xishuangbanna in Southwest China. *Environ. Sci. Pollut. Res.* **2021**, *28*, 40192–40202. [CrossRef] [PubMed]

56. Cao, Y.; Kong, L.; Ouyang, Z. Characteristics and Driving Mechanism of Regional Ecosystem Assets Change in the Process of Rapid Urbanization—A Case Study of the Beijing–Tianjin–Hebei Urban Agglomeration. *Remote Sens.* **2022**, *14*, 5747. [CrossRef]

57. Fan, C.; Chen, X.; Zhong, L.; Zhou, M.; Shi, Y.; Duan, Y. Improved Wallis Dodging Algorithm for Large-Scale Super-Resolution Reconstruction Remote Sensing Images. *Sensors* **2017**, *17*, 623. [CrossRef] [PubMed]

58. Zhao, L.; Li, Q.; Zhang, Y.; Wang, H.; Du, X. Normalized NDVI valley area index (NNVAI)-based framework for quantitative and timely monitoring of winter wheat frost damage on the Huang-Huai-Hai Plain, China. *Agric. Ecosyst. Environ.* **2020**, *292*, 106793. [CrossRef]

59. Zhao, Y.; Liu, D. A robust and adaptive spatial-spectral fusion model for PlanetScope and Sentinel-2 imagery. *Gisci. Remote Sens.* **2022**, *59*, 520–546. [CrossRef]

60. Ye, N.; Morgenroth, J.; Xu, C.; Chen, N. Indigenous forest classification in New Zealand-A comparison of classifiers and sensors. *Int. J. Appl. Earth Obs. Geoinf.* **2021**, *102*, 102395. [CrossRef]

61. Wang, Q.; Zhai, P.-M.; Qin, D.-H. New perspectives on 'warming–wetting' trend in Xinjiang, China. *Adv. Clim. Chang. Res.* **2020**, *11*, 252–260. [CrossRef]